Revision 1 MS 5328

The W-WO_2 oxygen fugacity buffer (WWO) at high pressure and temperature: Implications for fO_2 buffering and metal-silicate partitioning.

Gregory A. Shofner[1*], Andrew J. Campbell[2], Lisa R. Danielson[3], Kevin Righter[4], Rebecca A. Fischer[2], Yanbin Wang[5], and Vitali Prakapenka[5]

[1]Department of Physics, Astronomy and Geosciences, Towson University, 8000 York Road, Towson, MD 21252, USA

[2]The University of Chicago, Department of the Geophysical Sciences, 5734 South Ellis Avenue, Chicago, IL 60637, USA

[3]Jacobs Technology, NASA Johnson Space Center, 2101 NASA Parkway, Houston, TX 77058, USA

[4]Mailcode KT, NASA Johnson Space Center, 2101 NASA Parkway, Houston, TX 77058, USA

[5]Center for Advanced Radiation Sources, The University of Chicago, Building 434A, Argonne National Laboratory, 9700 South Cass Ave. Argonne, IL 60439

Abstract

Synchrotron x-ray diffraction data were obtained to simultaneously measure unit cell volumes of W and WO_2 at pressures and temperatures up to 70 GPa and 2300 K. Both W and WO_2 unit-cell volume data were fit to Mie-Grüneisen equations of state; parameters for W are K_T = 307 (±0.4) GPa, K_T' = 4.05 (±0.04), γ_0 = 1.61 (±0.03), and q = 1.54 (±0.13). Three phases were observed in WO_2 with structures in the $P2_1/c$, Pnma and C2/c space groups. The transition pressures are 4 GPa and 32 GPa for the $P2_1/c$-Pnma and Pnma-C2/c phase changes, respectively. The $P2_1/c$ and Pnma phases have previously been described whereas the C2/c phase is newly described here. Equations of state were fitted for these phases over their respective pressure ranges yielding the parameters K_T = 238 (±7), 230 (±5), 304 (±3) GPa, K_T' = 4 (fixed), 4 (fixed), 4 (fixed) GPa, γ_0 = 1.45 (±0.18), 1.22 (±0.07),

1.21 (±0.12), and q = 1 (fixed), 2.90 (±1.5), 1 (fixed) for the $P2_1/c$, Pnma and C2/c phases, respectively. The W-WO_2 buffer (WWO) was extended to high pressure using these W and WO_2 equations of state. The T-fO_2 slope of the WWO buffer along isobars is positive from 1000 to 2500K with increasing pressure up to at least 60 GPa. The WWO buffer is at a higher fO_2 than the iron-wüstite (IW) buffer at pressures lower than 40 GPa, and the magnitude of this difference decreases at higher pressures. This implies an increasingly lithophile character for W at higher pressures. The WWO buffer was quantitatively applied to W metal-silicate partitioning by using the WWO-IW buffer difference in combination with literature data on W metal-silicate partitioning to model the exchange coefficient (K_D) for the Fe-W exchange reaction. This approach captures the non-linear pressure dependence of W metal-silicate partitioning using the WWO-IW buffer difference. Calculation of K_D along a peridotite liquidus predicts a decrease in W siderophility at higher pressures that supports the qualitative behavior predicted by the WWO-IW buffer difference, and agrees with findings of others. Comparing the competing effects of temperature and pressure the results here indicate that pressure exerts a greater effect on W metal-silicate partitioning.

Keyword: high pressure, tungsten, oxygen fugacity buffer, equation of state, metal-silicate partitioning

Introduction

Knowledge of volumetric properties of metals and oxides at high pressure and temperature contributes to our understanding of metal–silicate equilibria within planetary interiors, the latter of which can exert a strong influence on the chemical potential of oxygen (or oxygen fugacity, fO_2). The coexistence of a metal and its oxide at equilibrium constitutes an oxygen buffer, and can be used in 1-bar or high pressure experimentation to control or calculate fO_2 (e.g., Cottrell et

al. 2009, 2010; Burkemper et al. 2012; Dobson and Brodholt, 1999; Rubie, 1999). A common example relevant to the deep Earth is the iron–wüstite (IW) buffer which is often used to control and measure the fO_2 of Fe-bearing experiments. However, in non Fe-bearing experiments where fO_2 similar to IW is desired or in cases requiring fO_2 conditions more oxidizing or reducing than IW, an alternative buffer must be used. The fO_2 of the W-WO_2 (WWO) buffer is equal to IW at approximately 1200 K (at 1 bar), and becomes more oxidizing with increasing temperature, becoming approximately one log unit higher at 2200 K. For this reason, the WWO buffer is well-suited to experiments where fO_2 similar to that of IW is required, e.g. Cottrell et al. (2009, 2010) controlled and calculated experimental fO_2 using the WWO buffer in Fe-free, W-bearing melting experiments.

Oxygen fugacity buffers can have significant pressure dependencies. The volume difference between the metal and oxide of a buffer is used to obtain fO_2 along the buffer at high pressures, and therefore differences in compressibility of the metal and oxide can result in significant deviations of calculated fO_2 relative to 1-bar. The WWO buffer has been studied at ambient pressure conditions and at temperatures up to approximately 1700K (O'Neill and Pownceby 1993), but it has no experimental constraints at high pressure. Extension of the 1-bar buffers for application to high pressure experiments or to the conditions of the deep Earth requires precisely determined phase volumes of the metal and oxide phases at high pressure (Campbell et al. 2009), which can be calculated using equations of state.

The equation of state of W has been determined using extensive high pressure and temperature experimental constraints (Houska, 1964; Grimvall et al., 1987; Dewaele et al. 2004; Dorogokupets and Oganov 2007). The equation of state of WO_2, however, is limited to room-temperature elastic parameters determined from a computational study with no experimental

constraints (Dewhurst and Lowther 2001). Known phases of WO_2 are a $P2_1/c$ structure at 1-bar (Bolzan et al. 1995) and a *Pnma* structure that was synthesized at 8 GPa and 1120 K and characterized by x-ray diffraction at 1-bar and room temperature (Sundberg et al. 1994). The $P2_1/c$ and *Pnma* structured phases will be referred to as *ap*-WO_2 and *hp*-WO_2 following the naming convention of Sundberg et al. (1994). Nothing is known experimentally about WO_2 at pressures and temperatures higher than the studied conditions of the *hp*-WO_2 phase, and consequently the behavior of the WWO buffer is imprecisely constrained at higher pressures. Therefore, we have conducted high pressure and high temperature experiments to characterize the WWO buffer. The data are also applied to better understand the thermodynamics of W partitioning between metal and silicate under magma ocean conditions. The experimental work to characterize the WWO buffer was conducted using both diamond anvil cell (DAC) and multi-anvil press (MAP) techniques in conjunction with synchrotron x-ray diffraction.

Synchrotron X-ray diffraction experiments

To obtain thermal equations of state (EOS) and oxygen fugacity buffers for the W-WO_2 system, x-ray diffraction data were collected on coexisting W and WO_2. The sample materials were mixtures of approximately 1:1 by weight of W:WO_2 using powders acquired from Alfa-Aesar (>99.9% pure). Room-temperature DAC compression experiments included Pt as a pressure standard and the mixture was approximately 1:1:1 by weight of W:WO_2:Pt. Powders were ground under ethanol in agate mortars to ~1 micron grain size for DAC experiments; for MAP experiments the powder mixtures were ground for approximately 15 minutes to homogenize the distribution of the phases. These data were collected across a wide range of pressures and temperatures (Figure 1) using diamond anvil cells at beamline X17C of the National Synchrotron Light Source (NSLS), Brookhaven National Laboratory, and using

diamond anvil cells and a multi anvil press at beamline 13-ID-D of the Advanced Photon Source (APS), Argonne National Laboratory. Making measurements of both metal and oxide in the same experiment was important because the oxygen fugacity buffer is defined in terms of the equilibrium between metal and oxide. It was also advantageous that both phases are present under the same experimental conditions in EOS calculations because the volume differences (ΔV) between the phases were referenced to exactly the same P-T conditions. This reduced or eliminated uncertainties due to pressure standardization and heterogeneous experimental conditions (P or T gradients) when coupling the two EOS for consideration of the metal-oxide buffer.

Diamond anvil cell

Room temperature compression provides the foundation for the thermal EOS. Coexisting W and WO_2 were compressed in DACs using an argon pressure medium over a pressure range of approximately 25 to 73 GPa. X-ray diffraction data were collected on beamline X17C at NSLS using angle-dispersive diffraction with diffraction patterns collected on a CCD (MAR) x-ray area detector. These x-ray diffraction data were used to determine unit cell volumes of the individual phases. Experimental pressures were determined using Pt as a pressure standard (Fei et al. 2007). The W data were included in the calculation of the W EOS as discussed in later sections. The room temperature WO_2 data were not included in EOS calculations because robust unit-cell volumes could not be obtained due to a sluggish phase transition from the *ap*-WO_2 to the *hp*-WO_2 phase at room temperature. As discussed in later sections, the *ap*-WO_2 and the *hp*-WO_2 phases coexisted over a pressure range of at least 20 GPa, which was evidenced by peaks for both phases in diffraction patterns over this pressure range.

Laser-heated DAC experiments were conducted at APS on coexisting W and WO_2 where x-

124 ray diffraction data were collected at temperatures up to approximately 2250 K and at pressures
125 up to approximately 70 GPa. The sample was prepared by compression of the starting mixture
126 into a thin layer that was ~5 μm thick. The sample was loaded into a symmetric-type DAC
127 between layers of NaCl that served as both insulator and as a pressure standard (Decker 1971;
128 Fei et al. 2007). The Pt pressure scale used in the 300 K experiments was calibrated with the
129 NaCl pressure scale used in the high temperature experiments – both used Fei et al. (2007). The
130 sample chamber was made by drilling an 80 micron hole in a pre-indented rhenium gasket and
131 was compressed between diamond anvils with 250 micron culet diameters. The monochromatic
132 x-ray source had a wavelength of 0.3344 Å and was focused to a spot size of ~3 μm diameter.
133 The diffraction data were measured using an angle-dispersive configuration and diffraction
134 patterns were collected using a MAR165 CCD x-ray area detector with the sample to detector
135 distance calibrated by 1-bar CeO_2 diffraction patterns. The sample was heated on both sides
136 using twin ytterbium fiber lasers with approximate spot sizes of 20 microns (Prakapenka et al.,
137 2008). Laser powers were adjusted to equalize the temperatures on the two sample surfaces. The
138 lasers were directed onto the sample using x-ray transparent optics which permitted the laser and
139 x-ray beams to be coaxial, and allowed for collection of x-ray diffraction data at high
140 temperatures (Shen et al. 2001). Temperatures were measured using spectro-radiometry and the
141 resulting thermal emission spectra were fitted to the Planck function using the greybody
142 approximation (Heinz and Jeanloz 1987). These measurements were of the temperature at the
143 interface between the sample and the insulating layer, i.e. at the surface of the sample, and over
144 an area of approximately 5 x 5 microns at the center of the laser-heated spot. The sample in this
145 experiment was opaque and most of the laser radiation was absorbed at the sample surface, and
146 consequently the temperature in the axial center of the sample where it was being probed by the

147 x-ray beam was slightly lower than the measured temperature. The reported experimental
148 temperatures were corrected for this axial thermal gradient, which was an approximately three
149 percent decrease from the measured temperatures, based on an approximate sample thickness of
150 5 microns (Campbell et al. 2007; 2009). Because of technical difficulties with the downstream
151 (relative to the x-ray beam) temperature measurements during these experiments, the
152 temperatures reported here are those measured in the upstream direction only (Fischer et al.,
153 2011). Four heating cycles were made, with starting pressures of approximately 18, 39, 53, and
154 67 GPa at ambient temperature; these are hereafter referred to as the 20, 40, 55, and 70 GPa
155 cycles. Laser power was gradually increased and diffraction patterns were collected up to the
156 peak temperature for a given pressure step. The laser power was then decreased gradually and
157 diffraction patterns were collected approximately every 100 degrees. The pressure in the
158 diamond cell was increased at room temperature between each heating cycle. The diffraction
159 data from the cooling portion of each heating cycle were used in EOS calculations to minimize
160 uncertainties related to non-hydrostatic stresses, which are greatly reduced after high temperature
161 treatment.

162 Resistively-heated DAC experiments (RHDAC) were made using an external heating system
163 that was developed in the University of Maryland Laboratory for Mineral Physics, which
164 allowed for sample chamber temperatures up to approximately 725 K. This heater design
165 completely enclosed a Tel-Aviv-type DAC, which minimized temperature gradients but caused
166 the pressure to decrease during heating. X-ray diffraction data were collected at beamline X17C
167 at NSLS using this DAC assembly. Diffraction patterns were collected at discrete temperatures
168 and at four different starting pressures. The sample was insulated between layers of NaCl, which
169 also served as a pressure calibrant (Decker 1971; Fei et al. 2007). Temperatures were measured

using a type K thermocouple that was placed at the contact between the diamond culets. This was done by wrapping the thermocouple loop around the diamonds and cementing the loop to the gasket using alumina cement obtained from Zircar Ceramics.

Multi anvil press

Diffraction patterns were collected using the T25 module in the 1000 ton MAP using a COMPRES octahedral 10/5 assembly (Leinenweber et al. 2006), at beamline 13-ID-D at the Advanced Photon Source. Boron nitride capsules were used because their low mean atomic number results in minimal attenuation of the x-ray beam, and samples were heated with Re or $LaCrO_3$ (Leinenweber et al., 2006, 2012) heaters. The entire cube assembly was aligned to allow the x-ray beam to pass between the gaps of the WC cubes, the "equatorial" graphite window, and slits in the Re and $LaCrO_3$ in the octahedral assembly. Diffracted x-rays were detected using a cooled Ge energy-dispersive detector placed at a fixed 2θ angle of 6° relative to the incoming x-ray beam.

The sample capsule had two chambers; one contained a mixture of W and WO_2, and the other contained MgO as a pressure calibrant. The equation of state for MgO of Speziale et al. (2001) was used and is compatible with the Pt and NaCl EOS of Fei et al. (2007) described above. An initial heating cycle was made at a press force of 800 tons corresponding to a pressure of approximately 20 GPa at 2100 K. Similar to LHDAC experiments, data were collected on the heating and cooling portions of this cycle but only the cooling data were used in EOS calculations. It was noted during the second cycle, at 400 tons press force, that the W diffraction peaks were weakening in relative intensity to those of WO_2. At this point the experiment was decompressed at constant temperature; data obtained at press forces of 350 and 270 tons were used in EOS calculations. Examination of the run product from this experiment revealed no W

193 metal, which suggests that the metal became oxidized over the course of the experiment which is
194 why the W diffraction intensities decreased so significantly. Tungsten carbide was not observed
195 either. The WO_2 remained a stable phase, consistent with successful indexing of the diffraction
196 data to the published orthorhombic (Pnma) structure (Sundberg et al. 1994). Microprobe
197 analyses of the WO_2 yielded W contents consistent with a stoichiometric phase, but future work
198 may want to examine this in more detail and for all three WO_2 phases.

199 **Data Analysis**

200 The foundational data for characterizing the equations of state were x-ray diffraction patterns
201 in the form of either two-dimensional CCD images or one-dimensional energy spectra collected
202 by a solid-state Ge, energy-dispersive detector. The 2-d diffraction patterns were calibrated with
203 CeO_2 and processed using the Fit2D software, which integrates a diffraction image to produce a
204 1-d spectrum of 2θ angle versus intensity (Hammersley et al., 1996). The 1-d energy dispersive
205 spectra were converted to *d*-spacing versus intensity spectra by applying energy and 2θ
206 calibrations. Energy calibrations were based on radioactive ^{57}Co and ^{109}Cd sources, and Ag K_α
207 and $K_{\beta 1}$ lines. The 2θ calibration was based on a 1-bar x-ray diffraction pattern of Al_2O_3. The x-
208 ray diffraction peaks in the experimental spectra were fitted using the PeakFit™ software by
209 SeaSolve Software Inc., which also allowed for background subtraction.

210 Because the difference in molar volume between the phases is used to calculate the fO_2 of the
211 WWO buffer, the principal information needed was the molar volumes of the W and WO_2 phases
212 at each P-T point. The molar volumes were calculated using the unit cell volumes and the
213 number of formula units per unit cell (Z).

214 Tungsten, sodium chloride, magnesium oxide, and platinum are cubic and for each reflection
215 a lattice parameter *a* was calculated from the measured *d*-spacings and the assigned Miller

indices $h\ k\ l$ by the equation, $a = d_{meas}\sqrt{h^2 + k^2 + l^2}$. The average of these calculated lattice parameters was taken as the lattice parameter for each phase in each pattern, and uncertainties were calculated as the standard error of the mean. See Supplementary Data for lattice parameters, and experimental pressures and temperatures (Table S1).

The pressure was calculated based on the equation of state of W (Dorogokupets and Oganov, 2007). Although other materials with well calibrated equations of state were included in each experiment (MgO in the MAP experiments; NaCl as the insulator / pressure medium in LHDAC/RHDAC experiments; Pt in room temperature DAC experiments), we found that the most reproducible results were obtained using W as the pressure standard, because it was intimately mixed with the WO_2 sample and at identical P–T conditions, whereas the same may not have been the case for MgO and NaCl. The primary difference in experimental conditions between W and either MgO or NaCl was likely temperature, i.e. slightly different physical location in the presence of a thermal gradient resulted in differences in thermal pressures in the phases. Consideration of the experimental configurations in comparison to the differences in pressures calculated using W and either MgO or NaCl supports this interpretation. For example in the MAP experiments the MgO was separate from but adjacent to the sample chamber, and the W and MgO pressures were largely consistent within uncertainties (~1 GPa). The temperature difference across this distance could have been up to approximately 100 K (Leinenweber et al. 2012), which would contribute to an approximately 0.5 GPa difference in calculated pressure of either W or MgO. The NaCl thermal gradient in the RHDAC experiments, in which the entire cell was heated, was likely less than 100 K, and the W and NaCl pressures were likewise consistent within uncertainties. In contrast, the axial thermal gradient through the NaCl layers in the LHDAC experiments was large with a correspondingly higher level of uncertainty on the

range of temperatures of the NaCl probed by the x-ray beam. In the room-temperature DAC experiments, some of the pressures calculated using Pt and W differed outside of uncertainties, probably because of nonhydrostatic stresses at low temperature.

Tungsten dioxide phases

Both monoclinic and orthorhombic WO_2 phases (*ap*-WO_2 and *hp*-WO_2) have been described in the literature (Bolzan et al. 1995, Sundberg et al. 1994). In the present experiments, both of these phases were observed in addition to a previously unpublished higher pressure and temperature monoclinic phase (*hpm*-WO_2 as described below). Miller indices were assigned to each identified peak in the patterns and lattice parameters were calculated using nonlinear least-squares minimization of the differences (Δd) of measured and calculated *d*-spacings.

In the crystal structures of both the *ap*-WO_2 and *hp*-WO_2 phases, the W atoms occupy one half of the octahedral sites. The *ap*-WO_2 structure is characterized by chains of W octahedra in a distorted rutile type structure. The *hp*-WO_2 structure is characterized as a twinned 1-bar structure (Sundberg et al. 1994). The W-W distances in the *hp*-WO_2 structure are shorter than in the *ap*-WO_2 structure by 0.5 to 0.7 Å. This contributes to the higher density of *hp*-WO_2 and therefore its thermodynamic stability at higher pressure.

The higher pressure monoclinic WO_2 phase (*hpm*-WO_2) was discovered during peak indexing of the LHDAC data. Comparison of peaks in the 20 GPa heating cycle were made to the 40 GPa heating cycle and it was apparent that the *Pnma*-structured *hp*-WO_2 phase was not present (Sundberg et al. 1994). The major orthorhombic peaks, (*111*) and (*230*) that were present in all 20 GPa patterns were absent in the 40 GPa and higher pressure data (Figure 2). Some similarities were observed between the 40, 55 and 70 GPa cycles, though additional peaks were present in the 55 and 70 GPa data suggesting that an additional phase was present at pressures

greater than 55 GPa. The diffraction pattern from this high pressure WO_2 phase was indexed using the method of successive dichotomy as coded in the DICVOL powder indexing software of Boultif and Louer (2004).

To assess the robustness of this method, DICVOL pattern indexing was conducted using the patterns from each of the temperatures in the 20 GPa cooling cycle. All solutions were in the orthorhombic crystal system, and ultimately solutions were obtained for multiple diffraction patterns that were in agreement with the *Pnma* structure of Sundberg et al. (1994). The diffraction spectrum for G33_006 (highest temperature pattern) compared to the 1-bar spectrum calculated using the Sundberg et al. (1994) structure data are shown in Figure 3. See Supplementary Data for lattice parameters, and experimental pressure and temperature conditions (Tables S2, S3 and S4).

Patterns from the 40 GPa data were likewise analyzed using DICVOL and all solutions were in the monoclinic system. The best solution was indexed with all Δd values less than 0.004 Å. This structure was in the *P2/m* space group and is here termed *hpm*-WO_2 (for high pressure monoclinic) following the convention of Sundberg et al. (1994). The *P2/m* space group of the *hpm*-WO_2 phase was the reduced cell form. A preferred space group *C2/c* was determined using the chekcell software (Laugier and Bochu).

Solutions determined using DICVOL for all W-oxide peaks in the 55 and 70 GPa data sets were not equivalent with the *hpm*-WO_2 of the 40 GPa set. This was likely due to a mixing of peaks from multiple phases. Peak indexing of the *hpm*-WO_2 phase was based on 16 to 19 peaks in the 55 GPa data and 7 to 12 peaks in the 70 GPa data. The uncertainties on the lattice parameters for the 70 GPa data were approximately twice that of the lattice parameters for the 55 GPa data because of larger Δd values and also fewer indexed peaks in the 70 GPa data. The

285 changes in density between the 40 and 55 GPa, and 55 and 70 GPa sets were approximately 3
286 and 4 percent, respectively, calculated along isotherms at 1000, 1300, 1700, and 2000 K.

287 Attempts were made to index the higher pressure (>40 GPa) data to a monoclinic WO_3
288 structure (Bouvier et al. 2002), under the hypothesis that WO_2 may have disassociated to WO_3
289 and metallic W. However, many prominent peaks could not be indexed and the calculated molar
290 volumes were not reasonable in comparison to the results of Bouvier et al. (2002). The proposed
291 orthorhombic unit cell of Dewhurst and Lowther (2001) also does not fit the high-P-T data
292 collected on WO_2.

293 Under room temperature compression and at approximately 25 GPa, a structural
294 transformation from monoclinic (*ap*-WO_2) to the orthorhombic structure of WO_2 was evident.
295 These two structures coexisted for at least 20 GPa, with the monoclinic phase (*ap*-WO_2) mostly
296 disappearing above approximately 45 GPa. Indexing the room temperature x-ray diffraction data
297 on the orthorhombic phase was not robust when referenced to either the Sundberg et al. (1994) or
298 Dewhurst and Lowther (2001) high pressure structures. Probable explanations include an
299 incomplete phase transition with a mixture of structural states, and structural distortions due to
300 accumulated strain related to room temperature compression.

301 High pressure x-ray diffraction experiments in a resistively-heated DAC conducted up to
302 approximately 42 GPa and at temperatures up to approximately 725 K also showed the
303 coexistence of the monoclinic (*ap*-WO_2) and orthorhombic (*hp*-WO_2) structured phases above 30
304 GPa. In the highest pressure, high-temperature data, the monoclinic and orthorhombic phases
305 appeared to have roughly equal contributions to the x-ray diffraction patterns as gauged by
306 relative peak intensities.

307 At higher temperatures the monoclinic (*ap*-WO_2)-to-orthorhombic (*hp*-WO_2) transition was

much faster. In our multi anvil press experiments and the lowest-pressure LHDAC experiments (<25 GPa), *hp*-WO_2 was easily identified. One or two diffraction peaks in the patterns from these experiments could possibly have been attributed to the *ap*-WO_2 phase, but the relative intensities of these peaks were extremely low. The *hp*-WO_2 phase was observed at a pressure of approximately 5 GPa and 300 K in the MAP experiments following a high temperature cycle. This suggests that the *ap*-WO_2 to *hp*-WO_2 transition has a kinetic barrier at 300 K, but *hp*-WO_2 is stable to low pressure and temperature conditions. This is also supported by the fact that Sundberg et al. (1994) recovered their *hp*-WO_2 phase to ambient conditions for x-ray diffraction analysis and crystal structure refinement. We place the phase boundary for the *ap*-WO_2 to *hp*-WO_2 transition at 4 GPa (near 400 K).

In the 40 GPa data from the LHDAC experiments, the *hpm*-WO_2 phase replaced the *hp*-WO_2 phase present in the 20 GPa data. Some of the peaks for *hpm*-WO_2 were present in the 55 GPa data, though other peaks in these data could not be indexed as *hpm*-WO_2 and represent a coexisting phase assumed to be another tungsten oxide. The intensity of W diffraction relative to the oxide decreased in this pressure range, suggesting that perhaps the second, non-*hpm*-WO_2 oxide phase was the result of the reduction of WO_2 and oxidation of W to form a lower valence tungsten oxide, perhaps W_2O_3 (W^{3+}). The intensity of WC diffraction remained nearly constant across the high pressure data. Plots of the highest temperature spectra from the 20, 40, 55 and 70 GPa data are shown in Figure 4, illustrating the changes in the phase complement in the LHDAC experiments. The diffraction spectra show the change in crystal structure observed for WO_2 from *Pnma* to *C2/c*, the decrease in W relative peak intensities, and the appearance of WC peaks at 40 GPa. The *hpm*-WO_2 phase was identified in both 29 GPa and 39 GPa diffraction patterns at 300 K (room temperature compression), but was entirely absent in the high temperature data in the 40

GPa range. This places the possible phase boundary between *hp*-WO_2 and *hpm*-WO_2 over a range of ~23 to 39 GPa. Lack of high temperature data in this pressure range leads to the simplest choice for the phase boundary at approximately 32 GPa. A phase diagram for W+WO_2 is shown in Figure 5.

During EOS fitting, described in the following section, the robustness of the *hpm*-WO_2 phase identification in the 70 GPa data was brought into question. The misfit of the 40, 55 and 70 GPa data were not randomly distributed and showed distinct groupings above and below the zero axis and the RMSE of the fit was approximately 2 GPa. Fit quality improved when not including the 70 GPa data with a reduction of the RMSE to 0.28 GPa. The additional oxide peaks in the 55 GPa data not belonging to the *hpm*-WO_2 phase were likely from another W-oxide phase. This other phase increased in abundance in the 70 GPa data evidenced by the increase in relative abundance of these peaks and a corresponding decrease in the W peaks. These observations may signal an incomplete phase transition in which the *hpm*-WO_2 phase was transforming to yet another WO_2 structure. Assuming this was this case, the decreased number of *hpm*-WO_2 peaks and increased lattice parameter uncertainties at 70 GPa was the result of a mixed-phase state similar to that observed in low temperature compression where coexisting *ap*-WO_2 and *hp*-WO_2 phases resulted in poorer quality lattice parameter fits for these phases. The 70 GPa were not included in the EOS fit for *hpm*-WO_2.

Finally, the temperatures and pressures of boundaries between the WO_2 phases (*P2/c*, *Pnma*, and C2/c) are not well constrained here (only at ~ 4 GPa and 300-500 K for *P2/c* and *Pnma*), and could be a focus of future investigations.

Tungsten Carbide

For the LHDAC experiments, tungsten carbide (WC) was present in all x-ray diffraction

spectra at pressures greater than 40 GPa. The source of the carbon to produce WC was likely from the diamond anvils during laser heating, as has been observed previously in laser heated experiments (e.g., Prakapenka et al. 2003). The diffraction peaks had low relative intensity and remained essentially the same intensity across the high pressure data sets. Lattice parameter values and unit-cell volumes are listed in Supplementary Data (Table S5). WC was also observed in diffraction data in the MAP experiments. Unlike the LHDAC experiments, the small WC peaks observed in multi-anvil runs are most likely due to C source in the assembly such as acetone or adhesive, rather than from the WC cubes or graphite x-ray windows in the assembly.

Results and discussion

Equations of state

Thermal equations of state (EOS) describe the relationship between pressure, temperature, and volume for a given phase. To calculate the WWO fO_2 buffer (see next section), a thermal EOS for each of the observed WO_2 phases and for W was needed. The P-V-T data for each phase were fit to Mie–Grüneisen equations of state,

$$P = P_{298}(V) + \left(\frac{\gamma}{V}\right)[E(\theta_D, T) - E_{298}(\theta_D, T = 298)] \quad (1)$$

where the room-temperature pressure component, P_{298}, is represented by a 3rd order Birch-Murnaghan EOS, and is a function of volume only; $P_{298} = 3K_T f(1+2f)^{5/2}(1+1.5(K_T^{'}-4)f)$, where K_T is the isothermal bulk modulus, K_T' is the bulk modulus pressure derivative, and the Eulerian strain (f) = $0.5\left(\left(V/V_0\right)^{-2/3}-1\right)$ with V = volume and V_0 = zero-pressure volume. A Debye model of vibrational energy, E, was used for the thermal pressure component which includes a Grüneisen parameter $\gamma = \gamma_0(V/V_0)^q$ and Debye temperature $\theta_D = \theta_0 exp[\gamma_0/q\,(1-(V/V_0)^q)]$ (see Figure S1). For hp-WO_2, the optimal solution is K_T = 230, γ_0 = 1.22 and q = 2.9 with K_T' = 4 fixed. Fixing q = 1, K_T' = 4, the best fit K_T = 222 and the best fit Grüneisen

parameter is γ_0 = 1.23. The difference in the r.m.s. misfits and the errors on the K_T and γ_0 parameters for these two fits are negligible. A fit with all four parameters free to vary resulted K_T = 226, γ_0 = 1.43, and q = 5.2 and K_T' unconstrained, which may reflect the relatively small pressure range of data containing this phase and an insufficient number of data to properly fit four parameters. For hpm-WO_2, the optimal solution is K_T = 304, γ_0 = 1.21 and V_0 = 18.072 with K_T' = 4 and q = 1 fixed; a similar fit with free K_T' resulted in a larger error on Vo and with K_T' approximately equal to four, and therefore K_T' was fixed at 4. A fit with all five parameters free to vary resulted identical K and γ_0 values, V_0 = 18.080, and q and K_T' unconstrained. Because of the relatively limited temperature range of the data for ap-WO_2, the overall fit was relatively insensitive to changes of the Grüneisen parameter. Setting γ_0 = 1 or 2 resulted in an increase of approximately 0.1 GPa r.m.s. misfit with the bulk modulus, K_T = 238, unchanged. These optimal equation of state parameters are listed in Table 1 and the equation of state for WO_2 is plotted along isotherms in Figure 6.

The EOS for W was used as the pressure calibration for our data from MAP and DAC experiments ranging 300 to 2250 K, and 2 to 72 GPa. We refitted the EOS of Dorogokupets and Oganov (2007) to a Mie–Grüneisen EOS. The resulting bulk modulus and pressure derivative were 307 (±0.40) GPa and 4.05 (±0.04) GPa, respectively, which compared well with the values 306 GPa and 4.17 GPa from Dorogokupets and Oganov (2007). The r.m.s. misfit of our refitted equation of state to the Dorogokupets and Oganov (2007) equation state was only 0.04 GPa over the pressure and temperature range of this study. The overall fit was optimized by inclusion of both thermal parameters. Fitting with q = 1 required a change in γ_0 of approximately 0.1 and increased the r.m.s. misfit by the same amount. Fixing γ_0 = 1.5 and q = 1 increases r.m.s. by approximately 0.1 GPa.

The W-WO_2 oxygen fugacity buffer (WWO)

With equations of state for both W and WO_2, the 1-bar WWO fO_2 buffer (O'Neill and Pownceby 1993) was extended to high pressures, which allowed for calculating the fO_2 at any P or T conditions (Campbell et al. 2009). The Gibbs free energy difference on the WWO buffer is

$$\Delta G_{WWO} = G_{WO_2} - G_W = RT ln f(O_2) \quad (2)$$

Given that $d(\Delta G) = -\Delta S dT + \Delta V dP$ and that $dT = 0$ along an isotherm,

$$\Delta G_{WWO(P,T)} = \int_{P=1bar}^{P} \Delta V dP + \Delta G^*_{WWO(P=1bar,T)} \quad (3)$$

which shows that the pressure dependence of the WWO buffer is related to the volume difference (ΔV) between W and WO_2. Combining Equations 2 and 3 gives:

$$\ln f(O_2) = \left(\ln f(O_2)_{1bar} + \int_{P=1bar}^{P} \Delta V dP \right) \Big/ RT \quad (4)$$

The WWO buffer was calculated over a pressure range of 1 bar to 70 GPa in 1 GPa increments and over a temperature range of 250 to 2500 K in 250 K increments. The 1-bar values were calculated using the equation of O'Neill and Pownceby (1993), $fO_2|_{WWO}$ = -596,087 + 300.5T - 15.97T * ln(T). Calculations above 1700 K were an extrapolation of the O'Neill and Pownceby (1993) data and were necessary for extension of the 1 bar buffer to higher pressures and temperatures. The fO_2 along the WWO buffer was calculated along isotherms for P > 1 bar using Equation 4 to generate a matrix of fO_2 values. The equations of state for W and WO_2 were inverted to determine the required ΔV values to solve the integral in Equation 4. Multiple WO_2 phases made it necessary to apply more than one equation of state. At equilibrium and along the *ap*-WO_2–*hp*-WO_2 and *hp*-WO_2–*hpm*-WO_2 phase boundaries, the chemical potentials of the coexisting phases are equal, and therefore the integration in Equation 4 was carried across these phase boundaries.

The calculations described above produced matrices of fO_2 values with isothermal rows and isobaric columns. These data are adequate for plotting curves, but to facilitate rapid calculation of the fO_2 of the WWO buffer at any P–T condition, the tabular (matrix) data were fit to three polynomial expressions, one each for the three WO_2 phases. The polynomial form used was, $log\, fO_2\, I_{WWO} = (A_0 + A_1P) + (B_0 + B_1P + B_2P^2)/T$. The temperature and pressure ranges of data used for the fits, and the $logfO_2 = (a_0 + a_1P + a_2P^2 + a_3P^3) + (b_0 + b_1P + b_2P^2 + b_3P^3)/T$fit parameters and the r.m.s. misfit are shown in Table 2. The WWO buffer was calculated along isobars using these expressions and these are plotted as a function of inverse temperature in Figure 7. Data points from the tabular data are plotted as points on Figure 7 to illustrate the quality of the fits. The fO_2 along the WWO buffer is positively correlated with temperature and pressure indicating that the system becomes more oxidizing at higher temperatures and pressures. The calculated logfO_2 values have very small slope change at the phase transitions in WO_2, but these are subtle; for example the different between the curves for the intermediate and high pressure WO_2 calculated at 50 GPa and 1073 K is ~ 0.5 log fO_2 unit.

The difference between the WWO and IW (Campbell et al. 2009) buffers is shown in Figure 8. At pressures lower than 40 GPa, the WWO buffer is at a higher fO_2 than the IW buffer. The magnitude of this difference decreases at higher pressures. The significance of this relationship between the WWO and IW buffers is that it predicts the siderophile character of W. The trend of decreasing siderophile character of W shown here suggests that W will trend toward more lithophile character with increasing pressure and therefore increasing depth within the mantle. As discussed in a later section the prediction of W metal-silicate partitioning based on experimental data agrees with this conclusion.

Our new results can be used in high pressure experimentation to constrain oxygen fugacity where a W capsule has been used (e.g. Cottrell et al., 2009). As one can see from our results (Figure 8) there is little difference in IW-WWO buffer change between 1 bar and 2 GPa, so there is no substantial correction to make to the work of Cottrell et al. (2009). However, if W capsules are used at pressures >20 GPa, the fO_2 should be calculated using our new EOS, because use of 1 bar data will result in erroneous fO_2.

Application to W metal/silicate partitioning

Following Campbell et al. (2009), the log of the exchange coefficient K_D for the Fe-W exchange reaction $2Fe + WO_2 = 2FeO + W$ as a function of the difference between the W-WO_2 and IW fO_2 buffers and the log of the ratio of activity coefficients is

$$logK_D - (logfO_2^{WWO} - logfO_2^{IW}) = log\left[\left(\gamma_{WO_2}^{sil}/\gamma_W^{met}\right)/\left(\gamma_{FeO}^{sil}/\gamma_{Fe}^{met}\right)^2\right] \quad (5)$$

Using the measured log K_D values from metal–silicate experiments and the calculated differences between the WWO and IW buffers at the P-T conditions of those experiments to calculate the left hand side, the right hand side can be rearranged as a sum of activity coefficients, which is related to the molar excess Gibbs energy of mixing of the Fe-W exchange reaction,

$G^{xs} = RT\sum_i log(\gamma_i) = RT\left(log\gamma_{WO_2}^{sil} - log\gamma_W^{met} - 2log\gamma_{FeO}^{sil} + 2log\gamma_{Fe}^{met}\right)$. Oxygen fugacity has a strong effect on W metal-silicate partitioning and this is addressed by the calculated difference of the WWO and IW buffers, which also contains most of the non-linear pressure dependence. We modeled the excess Gibbs energy of mixing to the first order with linear compositional, pressure and temperature dependencies

$$G^{xs} = RT\sum_i log\ (\gamma_i) = (H^{xs} - S^{xs}T + V^{xs}P)/RT + \sum_{i,j} z_i^j X_i^j \quad (6)$$

where i is a component in phase j with mole fraction X, and H^{xs}, S^{xs} *and* V^{xs} are the excess enthalpy, entropy and volume of mixing, respectively. The pressure dependence in the W, WO_2, Fe and FeO activity coefficients is contained in the excess molar volume of mixing term, V^{xs}.

Tungsten metal-silicate partitioning cast in terms of an Fe-W exchange partition coefficient is:

$$\log K_D = [logfO_2^{WWO} - logfO_2^{IW}] + \left[(H^{xs} - S^{xs}T + V^{xs}P)/RT + \sum_{i,j} z_i^j X_i^j\right] \quad (7)$$

The excess Gibbs energy of mixing was fitted for molar metal–silicate exchange partition coefficients that were calculated from literature data (Walter and Thibault, 1995; Hillgren et al., 1996; Ohtani et al., 1997; Righter and Shearer, 2003; Cottrell et al., 2009; Wade et al., 2012) and from unpublished data of Shofner et al. These partition coefficients were obtained from the measured mole fraction abundances of Fe and W in both the metallic and silicate phases. The phase components modeled as contributing to G^{xs} were SiO_2, Al_2O_3 and CaO in the silicate melt, and S in the metallic melt, and the results of this fit are shown in Table 3. It was assumed that the activity coefficients were the same for all WO_2 phases; this may be unlikely, but in the absence of any information otherwise we make this provisional assumption for these calculations.

The metal/silicate partitioning of W using Equation 7 was calculated along the peridotite liquidus, shown as curve B in Figure 9, and along isobars (Figure 10). A regression based on linear dependencies in all parameters is shown for comparison in Figures 9 and 10; the regression equation

$$log\ K_D = 2.00 - (3180 / T) - (125\ P / T) + (0.52\ X_C) - (4.27\ X_S) \quad (8)$$

was fitted to the data and calculated along the peridotite liquidus, where X_C and X_S are the mole fractions of carbon and sulfur, respectively, in the metallic Fe. Partitioning along the liquidus curves using Equations 7 and 8 have generally the same trend, with Equation 7 predicting a

491 larger decrease in the siderophility of W with increasing pressure. The slope change in curve B
492 at ~ 33 GPa is due to the difference in fO_2 calculated for the higher pressure form of WO_2.
493 Early work on W partitioning revealed non-ideality in both the metallic and silicate liquids (e.g.,
494 S and C content of metal (Jana and Walker, 1997a,b) and degree of polymerization in silicate
495 melt (Walter and Thibault, 1995)), making isolation of pressure effects difficult and perhaps
496 even unlikely. The agreement between our results on the pressure effects for the metal-oxide end
497 member and multi-component systems is perhaps unexpected and therefore worth highlighting
498 here.

499 Pressure and temperature have competing effects on the metal/silicate partitioning of W.
500 In the previous paragraph we have demonstrated that log K_D decreases at higher pressures. Yet,
501 calculated along isobars by Equation 7, log K_D is positively correlated with temperature where
502 the temperature effect is approximately 0.5 log units at 20 GPa, increasing to approximately 2.5
503 log units at 60 GPa between 2000 and 3000 K (Figure 10). However, in the more naturally
504 realistic case, along the peridotite liquidus where both pressure and temperature vary, pressure
505 exerts the greater effect. A comparison of Equation 7 to other predictive expressions of $K_D^{W(met-sil)}$
506 (Siebert et al. 2011; Wade et al. 2012) is shown in Figure 11. The prediction of Equation 7
507 (curve B) is similar to that of Siebert et al. (2011) (curve A) at lower pressures but the curves
508 diverge at higher pressures where the separation of the curves increases to 0.7 log units at 60
509 GPa. Wade et al. (2012) concluded that W metal-silicate partitioning has no significant pressure
510 dependence and this is shown by the essentially flat trend of curve C in Figure 11 across the
511 pressure range of 0 – 60 GPa. This is contrary to the findings of the present study and that of
512 Siebert et al. (2011). Using a predictive expression for log D_W from Cottrell et al. (2009, 2010)
513 and calculating W metal-silicate partitioning along the peridotite liquidus indicates an increase in

514 the lithophile behavior of W at higher pressures. While the Cottrell et al. (2009, 2010) expression
515 was not in terms of the Fe-W exchange coefficient, it results in the same trend of decreasing W
516 siderophile behavior at higher pressures.

517 The difference in the prediction of W metal-silicate partitioning by Equation 7 and
518 Siebert et al. (2011) is likely due to different approaches to modeling the pressure dependence of
519 fO_2, which has a strong influence on W metal-silicate partitioning. This is better characterized by
520 the measure of the volume difference between WWO and IW buffers as opposed to the simple
521 linear approximation of ΔIW. The pressure effect on fO_2 is captured by the equations of state
522 underlying the buffers that more precisely represent the volume changes at higher pressures
523 where non-linearity is more pronounced. The pressure dependence of W metal-silicate
524 partitioning is relatively small and therefore the difference between the linear and non-linear
525 (buffer-based) approaches is correspondingly small. However, it is likely that this difference
526 would be higher for other elements, e.g. Ni which has strong pressure dependence (Campbell et
527 al. 2009). Additional partitioning experiments at pressures higher than 30 GPa should also
528 improve the agreement between the two approaches (e.g., Shofner et al., 2014), since the
529 partitioning data is currently limited to pressures < 25 GPa.

530 **Implications**

531 Tungsten is a geochemically important element that has bearing on both the process and timing
532 of core formation in the Earth. The effect of the redox state of W on its geochemical behavior at
533 conditions of the deep Earth are crucial for accurate and precise determination of W properties
534 and behavior in core formation and other geochemical modeling. Extension of the 1-bar WWO
535 buffer to high pressures can improve its application in both deep Earth and high pressure
536 experimental applications. High pressure experimentation in this study identified a previously

unknown high-pressure phase of WO_2 that contributes to better understanding of the WWO buffer at high pressure. Applying the WWO buffer to metal-silicate systems can provide improved determination of the non-linear pressure effect on W metal-silicate partitioning, and of the activity of W in both silicate and metallic phases. The ultimate contribution of this work on the WWO buffer will be to improve constraints on Earth core formation models and to allow for the use of the WWO buffer in high pressure experiments by allowing more precise calculation of fO_2.

Acknowledgements

This research was supported by a NASA GSRP fellowship to GAS, NASA RTOP from the Cosmochemistry program to KR, and NSF grant EAR-1243847 to AJC. RAF was supported by the NSF GSFP and a Flagship Fellowship from University of Maryland. High pressure multi-anvil assemblies were produced by the COMPRES Infrastructure Development Project. Portions of this work were performed at GeoSoilEnviroCARS (Sector 13), Advanced Photon Source (APS), Argonne National Laboratory. GeoSoilEnviroCARS is supported by the National Science Foundation - Earth Sciences (EAR-1128799) and Department of Energy- GeoSciences (DE-FG02-94ER14466). This research used resources of the Advanced Photon Source, a U.S. Department of Energy (DOE) Office of Science User Facility operated for the DOE Office of Science by Argonne National Laboratory under Contract No. DE-AC02-06CH11357. Assistance with RHDAC experiments was provided by undergraduate researcher James Deane. Reviews by D. Walker, C. Lesher, and several anonymous reviewers helped improve the clarity of the manuscript.

559

560 **References cited**

561

562 Burkemper, L.K., Agee, C., and Garcia, K.A. (2012) Constraints on core formation from
563 molybdenum solubility in silicate melts at high pressure. Earth and Planetary Letters, 335, 95
564 – 104.

565 Boultif, A., and Louer, D. (2004) Powder pattern indexing with the dichotomy method. Journal
566 of Applied Crystallography, 37, 724 – 731.

567 Bolzan, A.A., Kennedy, B.J, and Howard, C.J. (1995) Neutron powder diffraction study of
568 molybdenum and tungsten dioxides. Australian Journal of Chemistry, 48, 1473-1477.

569 Bouvier, P., Crichton, W.A., Boulova, M., and Lucazeau, G. (2002) X-ray diffraction study of
570 WO_3 at high pressure. Journal of Condensed Matter, 14, 6605-6617.

571 Campbell, A.J., Seagle, C.T., Heinz, D.L., Shen, G., and Prakapenka, V.B. (2007) Partial melting
572 in the iron-sulfur system at high pressure: A synchrotron X-ray diffraction study. Physics of
573 the Earth and Planetary Interiors, 162, 119-128.

574 Campbell, A.J, Danielson, L., Righter, K., Seagle, C.T., Wang, Y., and Prakapenka, V.B. (2009)
575 High pressure effects on the iron-iron oxide and nickel-nickel oxide oxygen fugacity buffers.
576 Earth and Planetary Science Letters, 286, 556 – 564.

577 Cottrell, E., Walter, M.J., and Walker, D. (2009) Metal–silicate partitioning of tungsten at high
578 pressure and temperature: Implications for equilibrium core formation in Earth. Earth and
579 Planetary Science Letters, 281, 275-287.

580 Cottrell, E., Walter, M.J., and Walker, D. (2010) Erratum to Metal-silicate partitioning of
581 tungsten at high pressure and temperature: Implications for equilibrium core formation in the
582 Earth (vol 281, pg 275, 2009). Earth and Planetary Science Letters, 289, 631-634.
583 Decker, D.L. (1971) High-pressure equation of state for NaCl, KCl, and CsCl. Journal of
584 Applied Physics, 42, 3239.
585 Dewaele, A., Loubeyre, P., and Mezouar, M. (2004) Equations of state of six metals above 94
586 GPa. Physical Review B, 70, 094112.
587 Dewhurst, J.K. and Lowther, J.E. (2001) Highly coordinated metal dioxides in the cotunnite
588 structure. Physical Review B, 64, 014104.
589 Dobson, D. P., and Brodholt, J. P. (1999) The pressure medium as a solid-state oxygen buffer.
590 Geophysical Research Letters, 26, 259-262.
591 Dorogokupets, P.I., and Oganov, A.R. (2007) Ruby, metals, and MgO as alternative pressure
592 scales: a semiempirical description of shock-wave, ultrasonic, x-ray, and thermochemical
593 data at high temperatures and pressures. Physical Review B, 75, 024115.
594 Fei, Y., Ricolleau, A., Frank, M., Mibe, K., Shen, G., and Prakapenka, V. (2007) Toward an
595 internally consistent pressure scale. Proceedings of the National Academy of Science, 104,
596 9182 – 8186.
597 Fischer, R. A., Campbell, A. J., Shofner, G. A., Lord, O. T., Dera, P., and Prakapenka, V. B.
598 (2011) Equation of state and phase diagram of FeO. Earth and Planetary Science Letters 304,
599 496-502.
600 Goodenough, J.B., Hamnett, A., Huber, G., Hullinger, F., Leiß, M., Ramasesha, S.K., and
601 Werheit, H. (1984) Physics of Non-Tetrahedrally Bonded Binary Compounds III. Springer-
602 Verlag Berlin Heidelberg. 666 pages. ISBN 978-3-540-12744-4.

603 Grimvall, G., Thiessen, M., & Guillermet, A. F. (1987) Thermodynamic properties of tungsten.
604 Physical Review B, 36, 7816.
605 Hammersley, A.P., Svensson, S.O., Hanfland, M., Fitch, A.N., and Häusermann, D. (1996) Two-
606 dimensional detector software: from real detector to idealised image or two-theta scan. High
607 Pressure Research, 14, 235 – 248.
608 Heinz, D.L., and Jeanloz, R. (1987) Temperature measurements in the laser-heated diamond cell.
609 In Manghnani, M.H., and Y. Syono, Eds., High-Pressure Research in Mineral Physics.
610 Geophysical Monograph 29, Mineral Physics 2, American Geophysical Union, Washington,
611 D.C.
612 Herzberg, H., and Zhang, J., (1996) Compositions of magma in the upper mantle and transition
613 zone. Journal of Geophysical Research, 101 (B4), 8271-8295.
614 Houska, C.R. (1964) Thermal expansion and atomic vibration amplitudes for TiC, TiN, ZrC,
615 ZrN and pure tungsten. Journal of Physics and Chemistry of Solids, 25, 359-366.
616 Kittel, C. (1996) Introduction to Solid State Physics, 7th Ed., Wiley, New York.
617 Leinenweber, K., Mosenfelder, J., Diedrich, T., Soignard, E., Sharp, T. G., Tyburczy, J. A., and
618 Wang, Y. (2006) High-pressure cells for in situ multi-anvil experiments. High Pressure
619 Research, 26, 283-292.
620 Leinenweber, K., Tyburczy, J.A., Sharp, T.G., Soignard, E., Diedrich, T., Petuskey, W.B., Wang,
621 Y., and Mosenfelder, J. (2012) Cell assemblies for reproducible multi-anvil experiments (the
622 COMPRES) assemblies. American Mineralogist, 97, 353–368.
623 Laugier, J. and Bochu, B. CHEKCELL: graphical powder indexing helper and spacegroup
624 assignment software. Laboratoire des Materiaux et du Génie Physique de l'Ecole Supérieure
625 de Physique de Grenoble, France.

626 O'Neill, H.St.C, and Pownceby, M.I. (1993) Thermodynamic data from redox reaction at high
627 temperatures. I. An experimental and theoretical assessment of the electrochemical method
628 using stabilized zirconia electrolytes, with revised values for the Fe-"FeO", Co-CoO, Ni-
629 NiO, and Cu-Cu_2O oxygen buffers, and new data for the W-WO_2 buffer. Contributions to
630 Mineralogy and Petrology, 114, 296-314.
631 Prakapenka, V. B., A. Kubo, A. Kuznetsov, A. Laskin, O. Shkurikhin, P. Dera, M. L. Rivers, and
632 S. R. Sutton (2008) Advanced flat top laser heating system for high pressure research at
633 GSECARS: application to the melting behavior of germanium. High Pressure Research, 28,
634 225-235.
635 Righter, K., and Shearer, C.K. (2003) Magmatic fractionation of Hf and W: Constraints on the
636 timing of core formation and differentiation in the Moon and Mars. Geochimica et
637 Cosmochimica Acta, 67, 2497 – 2507.
638 Rubie, D.C. (1999) Characterising the sample environment in multianvil high-pressure
639 experiments. Phase Transitions: A Multinational Journal, 68, 431-451.
640 Shen, G., Rivers, M., Wang, Y., and Sutton, S. (2001) Laser heated diamond cell system at the
641 Advanced Photon Source for in situ x-ray measurements at high pressure and temperature.
642 Review of Scientific Instrumentations, 72, 1273-1282.
643 Shofner, G.A., Campbell, A.J., Danielson, L.R., Rahman, Z., and Righter, K. (2014) Metal-
644 Silicate Partitioning of Tungsten from 10 to 50 GPa. 45th Lunar and Planetary Science
645 Conference, abstr. # 1267.
646 Speziale, S., Zha, C-S., Duffy, T.S., Hemley, R.J, and Mao, H.K. (2001) Quasi-hydrostatic
647 compression of magnesium oxide to 52 GPa: implications for the pressure-volume-
648 temperature equation of state. Journal of Geophysical Research, 106, 515-528.

649 Sundberg, M., Werner, P.-E., and Zibrov, I.P. (1994) X-ray powder crystal structure analysis of
650 high pressure tungsten dioxide, on the information in weak reflections. Zeitschrift für
651 Kristallographie, 209, 662-666.
652 Wade, J., Wood, B.J, and Tuff, J. (2012) Metal-silicate partitioning of Mo and W at high
653 pressures and temperatures: Evidence for late accretion of sulphur to the Earth. Geochimica
654 et Cosmochimica Acta, 85, 57 – 74.
655 Walter, M.J., and Thibault, Y. (1995) Partitioning of Tungsten and Molybdenum between
656 metallic liquid and silicate melt. Science, 270, 1186 – 1189.
657 Zerr, A., Diegeler, A., and Boehler, R. (1998) Solidus of Earth's deep mantle. Science, 281, 243
658 – 246.
659

660 **Figure Captions**

661 **Figure 1.** Pressure and temperature distributions of x-ray diffraction experiments. MAP – multi-
662 anvil press, LHDAC – laser-heated diamond anvil cell, RHDAC – resistively-heated diamond
663 anvil cell, and DAC 300K – room-temperature compression in diamond anvil cell. The data
664 points are only those used in the EOS fit. There were higher pressure/temperature data collected,
665 but the limited number of peaks and the uncertainties on the volumes made the data unsuitable
666 for inclusion in the EOS.

667 **Figure 2.** X-ray diffraction spectrum showing patterns G33_006 and G33_022. The *hp*-WO_2
668 (*Pnma*) phase of WO_2 described by Sundberg et al. (1994) is present in spectrum 006 but is not
669 present in 022. The *d*-spacing offset between these two spectra is due to compression.

670 **Figure 3.** X-ray diffraction spectrum showing G33_006 and a calculated pattern for the *Pnma*
671 structure of the *hp*-WO_2 phase of WO_2 described by Sundberg et al. (1994). Peaks in high

672 pressure pattern offset in *d*-spacing by approximately -0.1 Å relative to 1-bar pattern due to
673 compression.

674 **Figure 4.** X-ray diffraction spectra from highest temperature pattern at each pressure range. The
675 *d-spacing* offset between the spectra is due to compression. The 110 and 211 peaks for W are
676 labeled to show the change in relative intensity of W to the other phases in the two highest
677 pressure data sets.

678 **Figure 5.** Phase diagram for WO_2. Space group of phases are indicated in italics. The green
679 symbol indicates the pressure and temperature synthesis conditions of the high pressure
680 orthorhombic phase (*Pnma*) described by Sundberg et al. (1994). Note that the overlap of data
681 near the *$P2_1/c$-Pnma* phase boundary is related to the low temperature phase dynamics as
682 discussed in the text. The various phases and space groups of WO_2 are: ap-WO_2 = $P2_1/c$; hp-
683 WO_2 = Pnma; hpm- WO_2 = C2/c. Color scheme is the same as in Figure 1.

684 **Figure 6.** PVT EOS for WO_2 plotted along isotherms as a function of pressure. Each phase is
685 plotted for the pressure ranges as shown in Figure 5. The various phases and space groups of
686 WO_2 are: ap-WO_2 = $P2_1/c$; hp-WO_2 = Pnma; hpm- WO_2 = C2/c.

687 **Figure 7.** Isobaric plot of the absolute fO_2 ($\log_{10}$) of the WWO buffer plotted as a function of
688 inverse temperature. Curves were calculated using the polynomial expressions in Table 2, and
689 the points are the fitted data from the tabulated values resulting from the extension of the 1-bar
690 WWO buffer to high pressure.

691 **Figure 8.** Difference between WWO and IW buffers plotted as isobars as a function of inverse
692 temperature. WWO was calculated using the polynomial expressions in Table 2, and IW was
693 calculated using the Fe-FeO buffer of Campbell et al. (2009).

694 **Figure 9.** The predicted W metal/silicate partitioning in terms of the $\log_{10}$ of the Fe-W exchange

coefficient calculated along a peridotite liquidus (Herzberg and Zhang 1996; Zerr et al. 1998). The red curve (B) was calculated using Equation 7, and for comparison, the blue curve (A) was calculated using Equation 8. The slope change in curve B at ~ 33 GPa is due to the difference in fO_2 calculated for the higher pressure form of WO_2.

Figure 10. Isobaric plots of the predicted W metal/silicate partitioning in terms of the log of the Fe-W exchange coefficient. Solid lines were calculated using Equation 7, and dotted lines were calculated using Equation 8.

Figure 11. Comparison of log K_D^W calculated along the peridotite liquidus as predicted by Siebert et al. (2011) (Curve A), Equation 7 (curve B), and Wade et al. (2012) (Curve C). The liquidus is a fit to data from Herzberg and Zhang (1996) and Zerr et al. (1998).

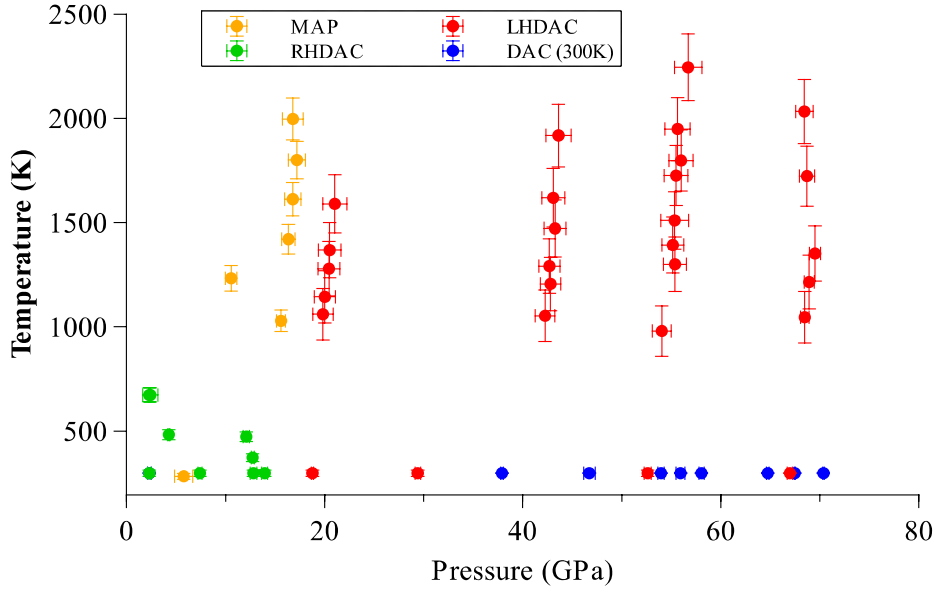
MAP
RHDAC
LHDAC
DAC (300K)
Temperature (K)
2500
2000
1500
1000
500
0
20
40
60
80
Pressure (GPa)

Figure 1

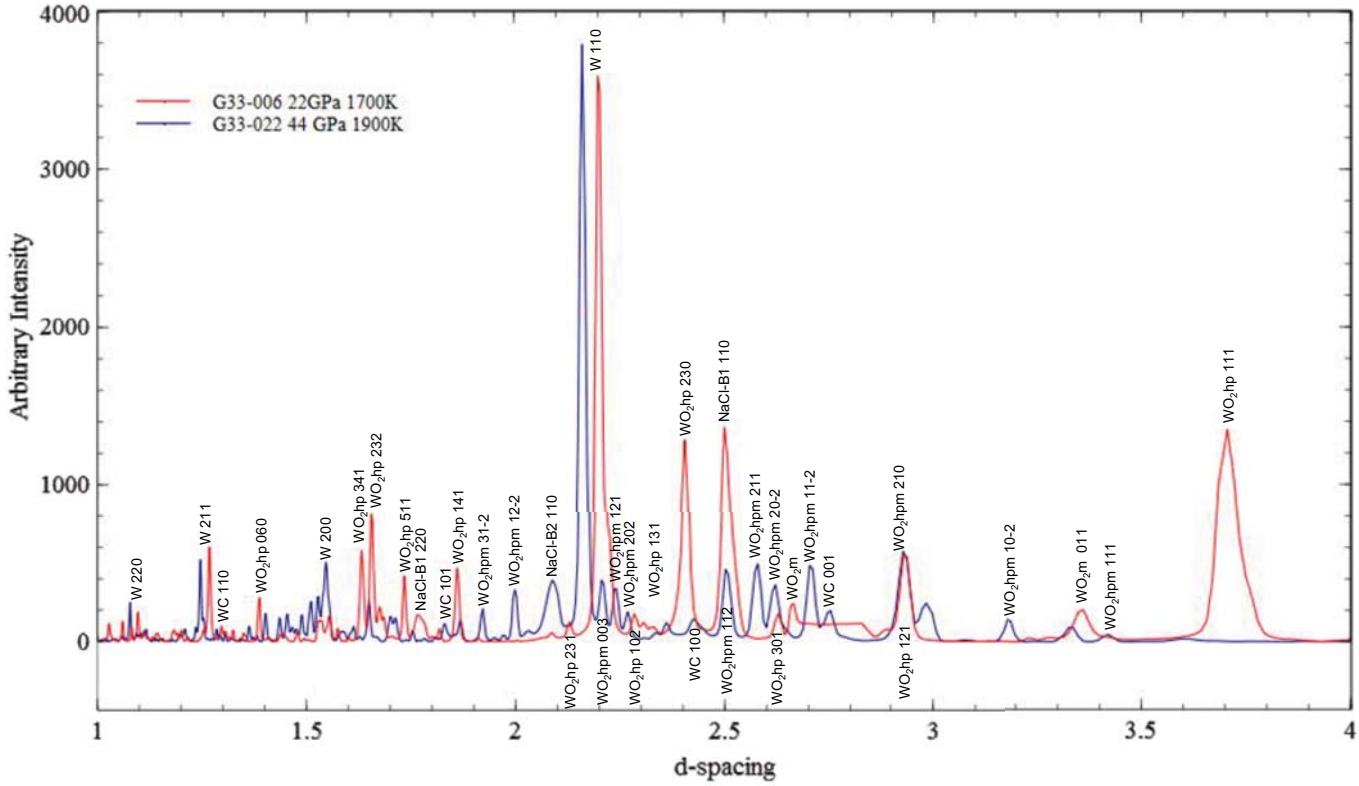
G33-006 22GPa 1700K
G33-022 44 GPa 1900K
Arbitrary Intensity
d-spacing
4000
3000
2000
1000
0
1
1.5
2
2.5
3
3.5
4
W 220
W 211
WC 110
WO2hp 060
W 200
WO2hp 341
WO2hp 232
WO2hp 511
NaCl-B1 220
WC 101
WO2hp 141
WO2hpm 31-2
WO2hpm 12-2
NaCl-B2 110
WO2hp 231
W 110
WO2hpm 003
WO2hpm 121
WO2hpm 202
WO2hp 102
WO2hp 131
WC 100
WO2hp 230
WO2hpm 112
NaCl-B1 110
WO2hpm 211
WO2hpm 20-2
WO2m
WO2hpm 11-2
WC 001
WO2hp 301
WO2hpm 210
WO2hp 121
WO2hpm 10-2
WO2m 011
WO2hpm 111
WO2hp 111

Figure 2

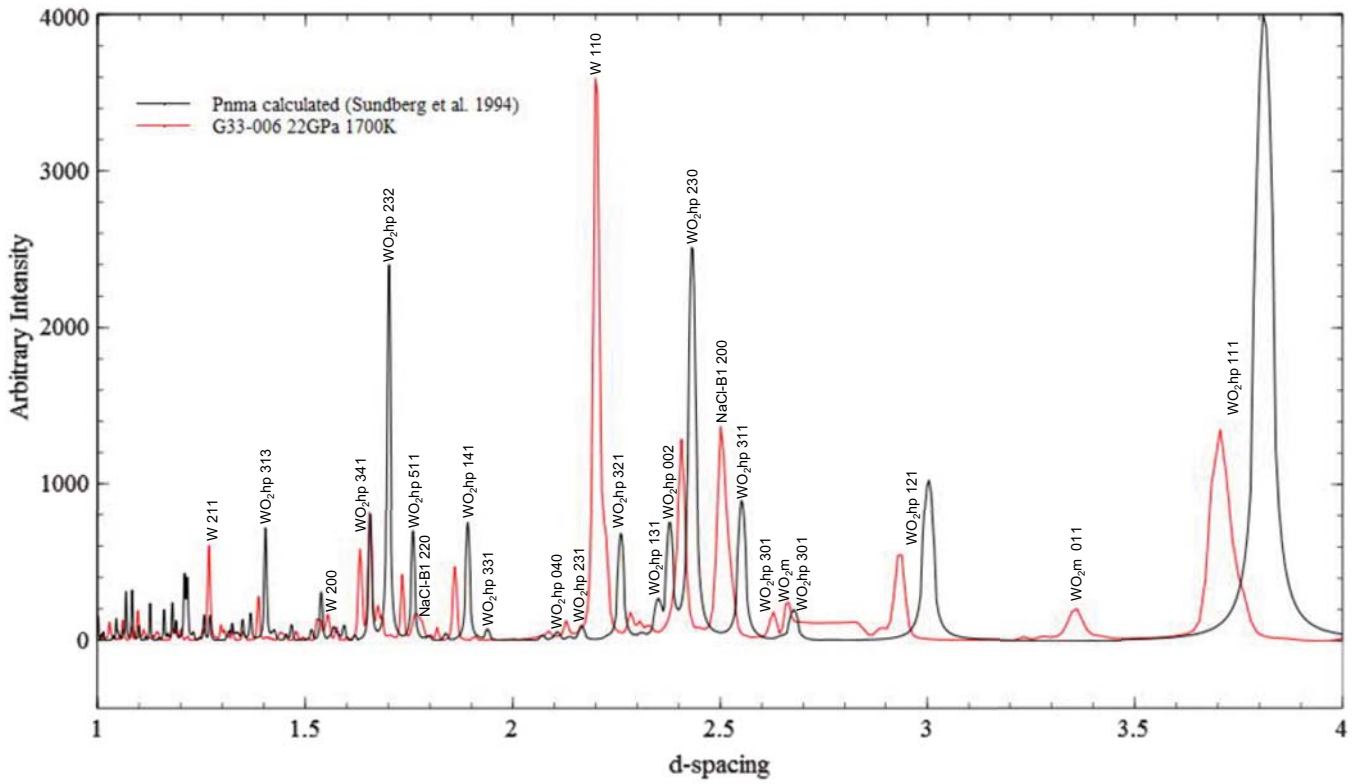
Pnma calculated (Sundberg et al. 1994)
G33-006 22GPa 1700K
Arbitrary Intensity
d-spacing
W 211
WO2hp 313
W 200
WO2hp 341
WO2hp 232
WO2hp 511
NaCl-B1 220
WO2hp 141
WO2hp 331
WO2hp 040
WO2hp 231
W 110
WO2hp 321
WO2hp 131
WO2hp 002
WO2hp 230
NaCl-B1 200
WO2hp 311
WO2hp 301
WO2m
WO2hp 301
WO2hp 121
WO2m 011
WO2hp 111

Figure 3

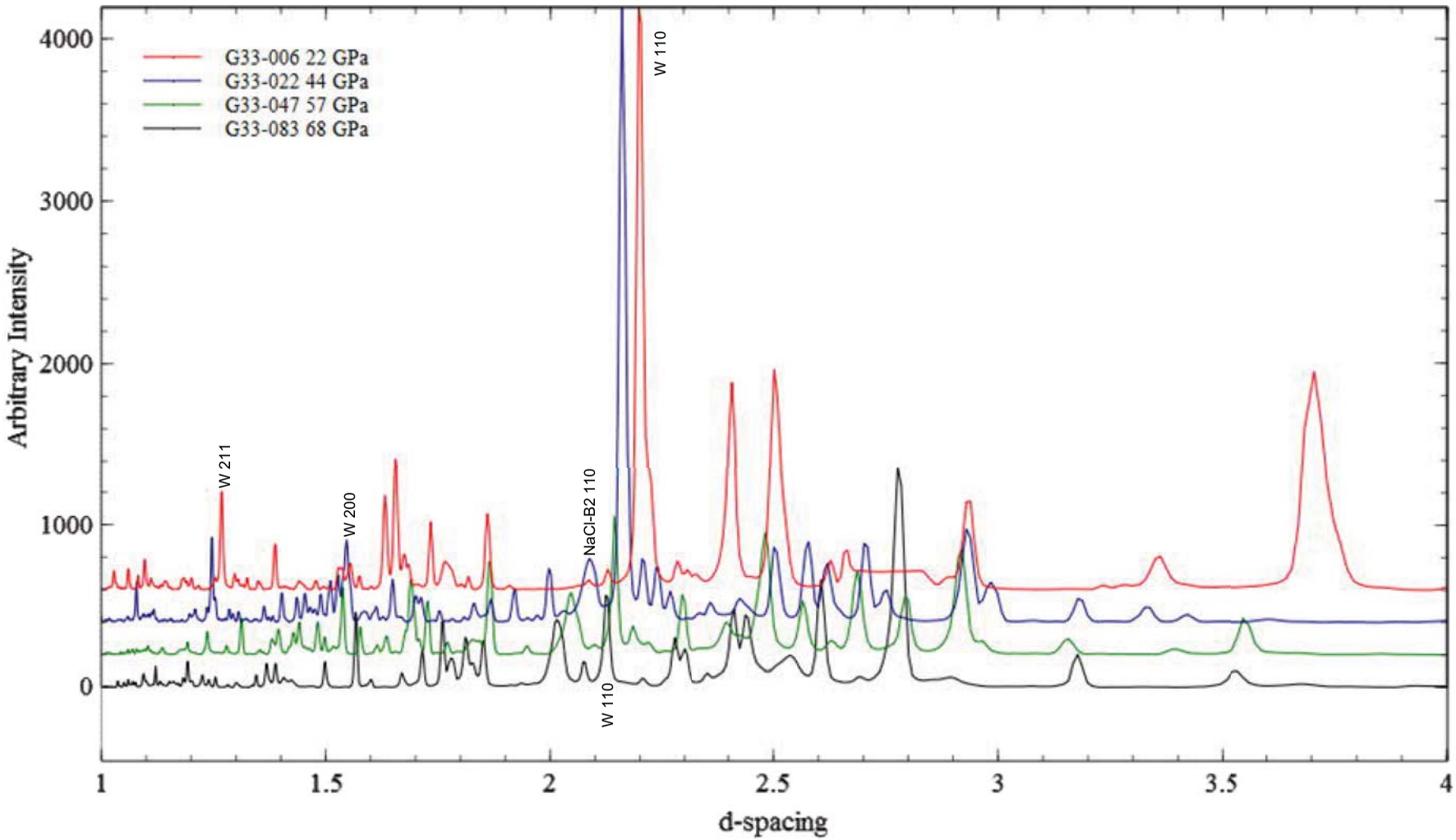
G33-006 22 GPa
G33-022 44 GPa
G33-047 57 GPa
G33-083 68 GPa
Arbitrary Intensity
d-spacing
W 211
W 200
NaCl-B2 110
W 110
W 110
0
1000
2000
3000
4000
1
1.5
2
2.5
3
3.5
4

Figure 4

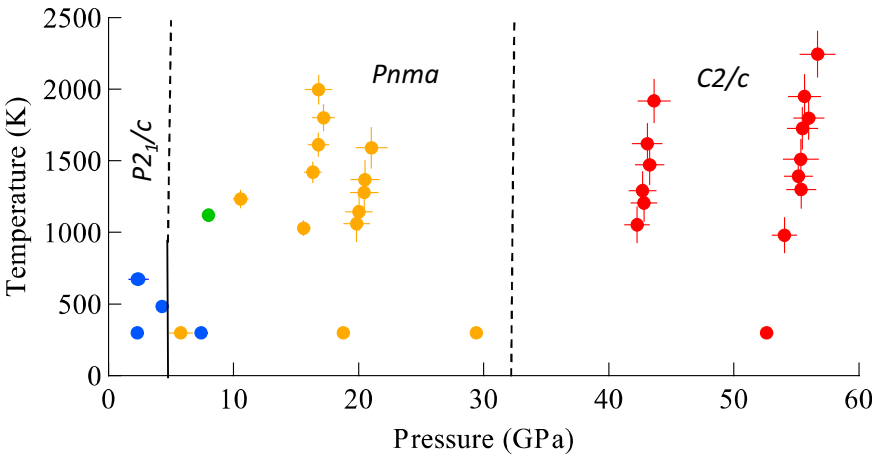
2500
2000
1500
1000
500
0
Temperature (K)
0
10
20
30
40
50
60
Pressure (GPa)
P2₁/c
Pnma
C2/c

Figure 5

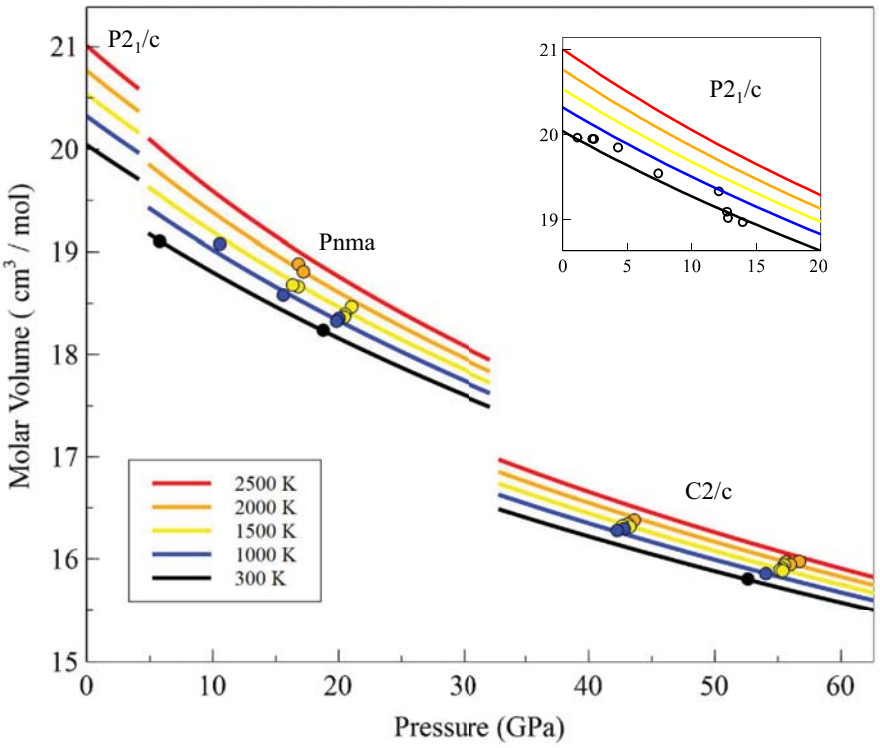
P2$_1$/c
Pnma
C2/c
2500 K
2000 K
1500 K
1000 K
300 K
Molar Volume (cm^3 / mol)
Pressure (GPa)
0
10
20
30
40
50
60
15
16
17
18
19
20
21
P2$_1$/c
0
5
10
15
20
19
20
21

Figure 6

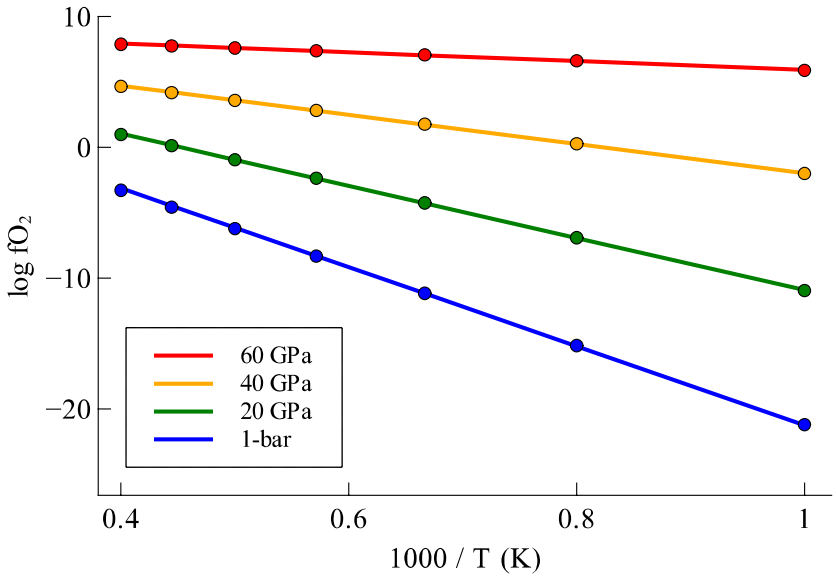

Figure 7

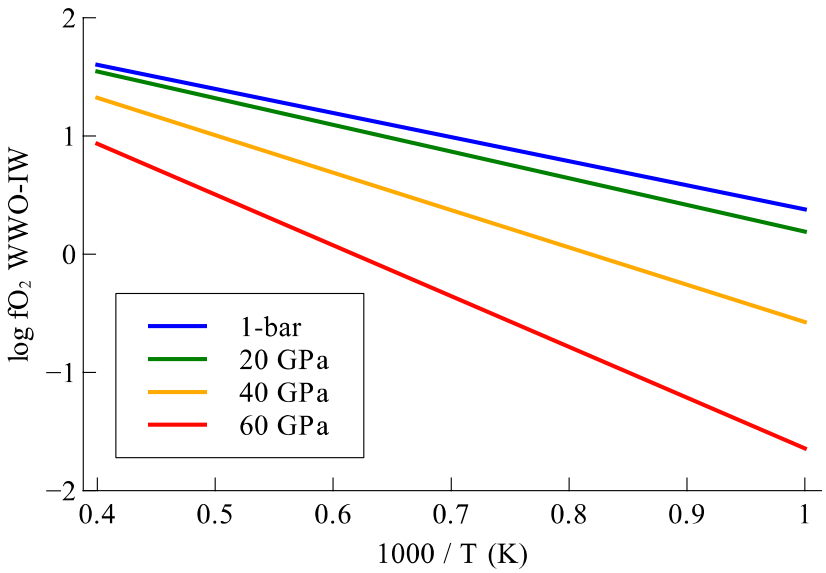
2
1
0
−1
−2
log fO2 WWO-IW
0.4
0.5
0.6
0.7
0.8
0.9
1
1000 / T (K)
1-bar
20 GPa
40 GPa
60 GPa

Figure 8

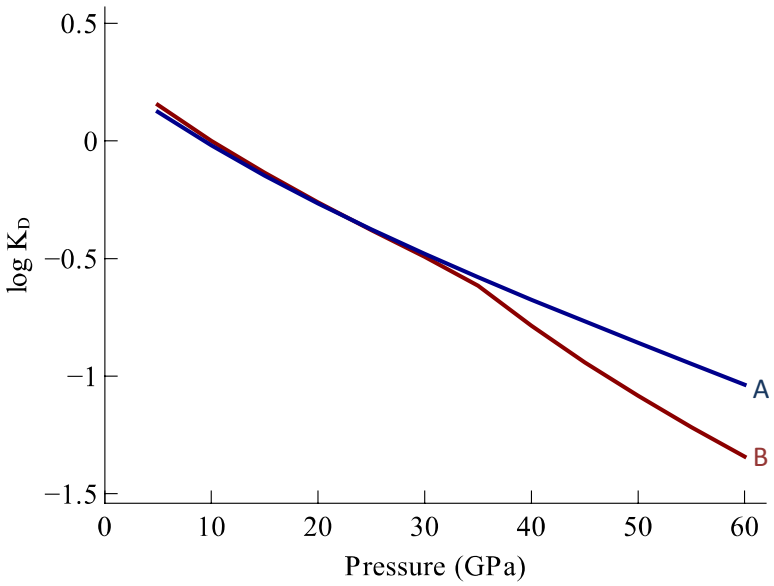

Figure 9

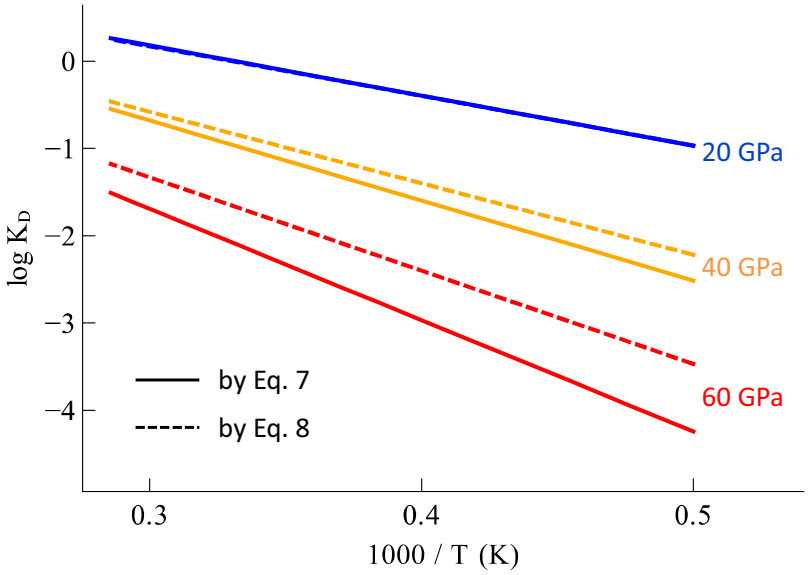

Figure 10

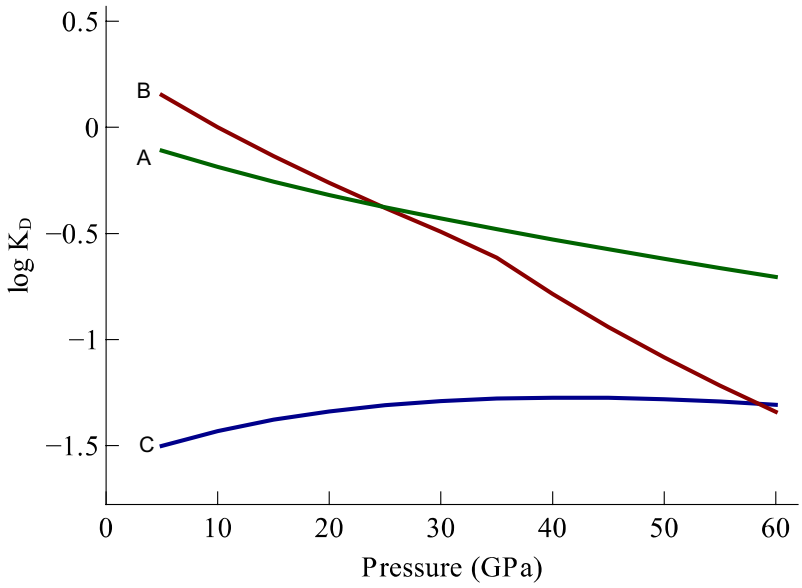

Figure 11

Table 1. Equation of state parameters (Birch-Murnaghan with Grüneisen parameter and Debye temperature).
[a]JCPDS card files. [b]Sundberg et al. (1994). [c]Kittel (1996). [d]Goodenough et al. (1984)

	W	ap-WO_2	hp-WO_2	hpm-WO_2
V_0 (cm^3/mol)	9.544[a]	20.037[a]	19.570[b]	18.072 ± 0.02
K_T (GPa)	307 ± 0.40	238 ± 4	230 ± 3	304 ± 3
K_T' (GPa)	4.05 ± 0.04	4 (fixed)	4 (fixed)	4 (fixed)
θ_D (K)	400[c]	380 ± 15[d]	380 ± 15[d]	380 ± 15[d]
γ_0	1.61 ± 0.03	1.45 ± 0.18	1.22 ± 0.07	1.21 ± 0.12
q	1.54 ± 0.13	1 (fixed)	2.90 ± 1.5	1 (fixed)
r.m.s. (GPa)	0.04	0.38	0.22	0.14

Table 2. Parameters of polynomial fits of tabulated fO_2 values for *P2 $_1$/c* , *Pnma* , and *C2/c* WO_2 phases in the high pressure W-WO_2 buffer.

$\log fO_2 |_{WWO} = (A_0 + A_1P) + (B_0 + B_1P + B_2P^2)/T$.

WO_2 phase	Parameters				r.m.s.	P range (GPa)	T range (K)
ap-WO_2 ($P2_1/c$)	A_0	8.957	B_0	-30200	0.023	0 - 4	750 - 2000
	A_1	0	B_1	554.2			
			B_2	0			
hp-WO_2 (Pnma)	A_0	8.860	B_0	-29947	0.018	5 - 32	1000 - 2250
	A_1	0.007804	B_1	524.1			
			B_2	-1.178			
hpm-WO_2 (C2/c)	A_0	9.000	B_0	-27954	0.027	33 - 70	1000 - 2250
	A_1	0.004493	B_1	438.8			
			B_2	-0.479			

Table 3. Fit parameter for the excess Gibbs energy of mixing in the W-WO2 buffer-based expression of the Fe-W exchange coefficient.

H^{XS}	-8.98 ± 7.8
S^{XS}	0.0236 ± 0.0036
V^{XS}	-1.02 ± 0.14
$zSiO_2$	6.58 ± 0.56
zAl_2O_3	7.02 ± 1.3
zCaO	-8.27 ± 1.0
zS	-4.49 ± 0.72
r.m.s.e.	0.26